Enhanced Transport into and out of Dead-End Pores

Abhishek Kar,[†] Tso-Yi Chiang,[†] Isamar Ortiz Rivera,[‡] Ayusman Sen,[*,‡] and Darrell Velegol[*,†]

[†]Department of Chemical Engineering, and [‡]Department of Chemistry, The Pennsylvania State University, University Park, Pennsylvania 16802, United States

ABSTRACT Dead-end micro- and nanoscale channels are ubiquitous in nature and are found in geological and biological systems subject to frequent disruptions. Achieving fluid flows in them is not possible through conventional pressure-driven mechanisms. Here we show that chemically driven convective flows leading to transport in and out of dead-end pores can occur by the phenomenon of "transient diffusioosmosis". The advective velocity depends on the presence of an *in situ*-generated transient ion gradient and the intrinsic charge on the pore wall. The flows can reach speeds of 50 μm/s and cause extraction of otherwise-trapped materials. Our results illustrate that chemical energy, in the form of a transient salt gradient, can be transduced into mechanical motion with the pore wall acting as the pump. As discussed, the phenomena may underlie observed transport in many geological and biological systems involving tight or dead-end micro- and nanochannels.

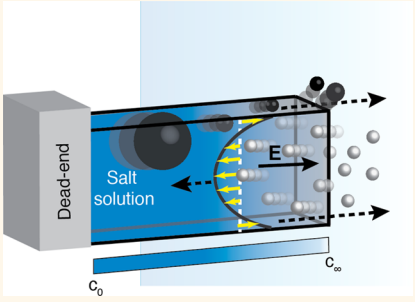

KEYWORDS: dead-end pore · diffusioosmosis · diffusiophoresis · transient ion gradient · mixing

Transport in dead-end micro- and nanoscale channels lies at the heart of many geological and biological phenomena. As an example, the introduction of low salinity water into reservoirs, has been shown to result in the enhanced recovery of oil stuck inside dead-end geological channels.[1,2] Salt diffusion across these channels appears to be critical for the recovery process.[3] Disturbances in the earth's crust, caused from earthquakes or drilling, have also been found to generate flows across cracks and fissures and have been correlated with the simultaneous observation of spontaneous electric potentials (SP).[4−7] In biology, transport in dead-end pores has been implicated in extra-cellular diffusion in brain tissue[8] and intratissue diffusion of water and biomolecules in muscles.[9]

Transport in dead-end pores through conventional pressure-driven flow is not possible.[10−13] Electric fields can cause flows in channels,[14−17] but in remote regions it is difficult to apply an external electric field. Designing conditions for chemically induced transport and fluid flow[18,19] has been challenging. However, the presence of electrolyte gradients (analogous to thermal gradients[20]) in the systems discussed suggests the critical role of electrokinetics, and specifically diffusioosmosis,[21−24] in driving flows in such geometries. Here we address the question: Is it possible to harness the presence of salt gradients to drive transport of materials *both* into and out of such pores? Experimentally, we find ion gradients can *simultaneously* move material in opposite directions in a *cul-desac* facilitating exchange of materials. Further, our electrokinetic model allows quantitative predictions that agree with these experimental observations.

RESULTS AND DISCUSSION

To simulate flows in a laboratory setting, a series of systematic experiments were performed with dead-end pores made of glass capillaries (Figure 1A, Supporting Information, Figure S1). We studied *transient diffusioosmotic flows* (TDOFs) that resulted from imposed salt gradients. To mimic natural systems, our salt gradients were time-dependent[25] and arose from both diffusion and convection of ionic species. The gradients give rise to spontaneous electric fields (**E**, eq 1) that generate transport near a charged surface or of charged particles.[21,26−29]

$$\mathbf{E} = \frac{kT}{Ze}\frac{D_+ - D_-}{D_+ + D_-}\frac{\nabla n}{n} \qquad (1)$$

Here, k is Boltzmann's constant, T is temperature, e is the proton charge, Z is the

* Address correspondence to asen@psu.edu, velegol@psu.edu.

Received for review October 31, 2014 and accepted January 5, 2015.

Published online January 05, 2015
10.1021/nn506216b

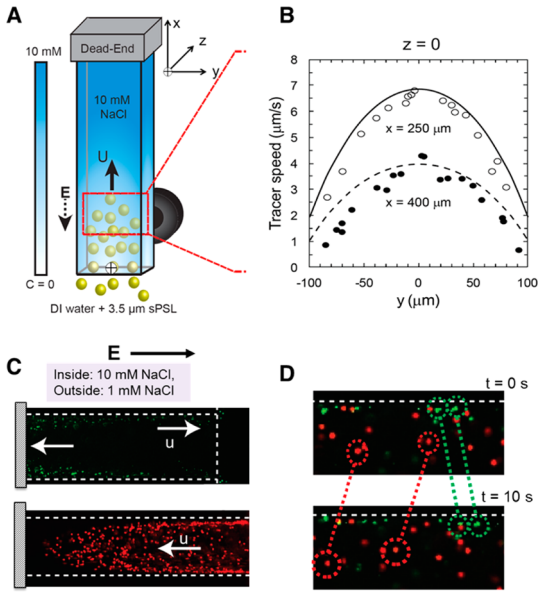

Figure 1. Particle transport and exchange of material into and out of dead-end pores due to TDOFs. (A) Experimental setup used to study transport rates of sPSL beads in dead-end pores. Experiments involved a simple vertical sink-reservoir model, containing a smaller capillary that serves as the salt reservoir, within a larger capillary containing only DI water. The solid black arrow indicates the direction of material transport and the black dashed line gives the E-field in the system. Direct visualization of material transport in these dead-end pores was done near the opening of the inner capillary (red open box). (B) The beads were transported upward against gravity both in the center and along the wall of the dead-end pore. Quantitative predictions of tracer speeds from electrokinetic modeling (represented by the curves), at different distances (x) into the dead-end pore are compared with experimental results (represented by open and closed circles) at t = 200 s. ζ_p = −101 mV and ζ_w = −65 mV. (C) Bottom: 4.0 μm red sPSL beads show diffusiophoretic transport toward the high salt regime both at the center and along the walls. Top: 2.0 μm green amine-functionalized PSL beads shows diffusiophoretic transport along the wall toward the sink whereas in the center, they move toward the dead-end region containing salt (toward left). (D) Upon adding red sPSL beads in the outside capillary and green amine-functionalized PSL beads in the inside capillary, exchange of material was observed. Near to the side walls of the dead-end pore (inner capillary), the green amine-functionalized PSL beads, initially inside, move toward the sink and eventually out of the pore, whereas the red sPSL beads, initially outside, move in and, eventually, fill up the entire inner capillary.

valence of a symmetric Z:Z electrolyte, n is the local salt concentration, and D_+ and D_- are the diffusion coefficients of the cation and the anion, respectively. At low salt concentrations where the classic electrokinetic theories hold,[30] the magnitude of this electric field depends on the difference in diffusion coefficients of the ions and the length over which the gradient is set up. The magnitudes of **E** can be as high as several V/cm. Aside from the **E**-field generated in the system that induces fluid and particle motion, double layer polarization due to chemical gradient (usually called chemiphoresis[28,31]) can also generate transport. The chemiphoretic contribution to transport rates is typically small; however, for completeness we have chosen to include it in our modeling. We explored the above phenomena experimentally using tracer particles (negatively charged polystyrene latex (PSL) beads with diameters of 4 and 2 μm) and oil emulsions. The 4 μm PSL beads were sulfate functionalized (referred to as sPSL beads), whereas the 2 μm PSL beads were amine functionalized. The ion gradients were produced by setting up a source and sink for our salt using concentric square capillaries, each closed at one end. Specifically, this involved a 20 mm × 0.20 mm capillary placed inside another 50 mm × 0.90 mm capillary (see Supporting Information, Figure S1). Typically the inner capillary was the source (higher salt concentration) and the outer one the sink (lower salt concentration or even deionized water). The tracers were added to the outer capillary. Details are available in the methods section. A vertical arrangement of the capillaries allowed us to avoid density-driven convective flows (see Supporting Information, Figure S2) in the system. While electrokinetic flows exhibit a nearly plug-flow profile in open channels, we observed a parabolic flow since our capillaries are closed at opposite ends, causing a pressure-driven back flow.

The **E**-field generated due to the salt gradient results in an electroosmotic fluid flow near the wall and a concurrent electrophoretic migration of the tracers (Supporting Information, Video S1) that is independent of electroosmotic flow.[32−34] The net observed transport rate is a combination of these two effects (see eq 2 and Supporting Information). Knowing **E**-field, the speeds of the tracers in the system can be predicted quantitatively, and by strategic placement in a salt gradient, we can control their movement toward or away from the salt-rich region. There are three critical parameters controlling the motion: (1) a finite difference in diffusivities of the two ions present in the salt ($D_+ - D_-$), (2) a finite surface potential, given by the zeta potential ζ, and (3) an electrolyte concentration gradient, ∇n. Precise control of these parameters can lead to a quantitative exchange of material across dead-end pores.

The speeds of the sPSL beads were analyzed using video microscopy in the xy plane with center of capillary at z = 0 (Figure 1A). In our experiments the **E**-field is directed from high to low NaCl concentrations (*i.e.*, along the negative direction of the x-axis). This is readily seen from eq 1, since $D_{Na+} = 1.334 \times 10^{-9}$ m^2/s and $D_{Cl-} = 2.032 \times 10^{-9}$ m^2/s. The initial speed we measured, up to 55 μm/s, was large close to the mouth of the dead-end-capillary and decreased with time and distance as the beads are transported into the smaller capillary. In Figure 1C, the less negative amine-functionalized PSL beads (green), in 10 mM NaCl have a zeta potential ($\zeta_p \approx -22$ mV) lower than that of the wall ($\zeta_w \approx -55$ mV), whereas the sPSL beads (red) have a higher zeta potential ($\zeta_p \approx -100$ mV) compared to

that of wall (ζ_w). Thus, the purely electrophoretic migration velocity for the green amine-functionalized PSL beads is less than that for red sPSL beads, with the magnitude of electroosmotic velocity near the wall lying in between the two. Hence, electroosmosis dominates in the former while electrophoretic migration controls net motion in the latter. As a result, for sPSL beads, the net movement is toward the higher salt regime, both along the wall and in the center (*i.e.*, in the direction of the dead-end) (Supporting Information, Video S2), while the amine-functionalized PSL tracers move toward the sink along the wall of the capillary and toward the higher salt concentration in the center (Supporting Information, Video S3). When combined in one setup, with the amine-functionalized PSL beads inside the dead-end inner capillary and the sPSL beads on the outside, we found these particles undergo exchange along the wall (Figure 1D, Supporting Information, Video S4). As expected, the rate of exchange varies with space and time due to the transient nature of the gradient. Similar trends are also observed with tracers of different sizes and zeta potentials which confirm our observation of TDOFs in the system (see Supporting Information, Figure S3). Since the effects in our dead-end-capillary system are transient in nature, we do anticipate ζ potentials to vary in magnitude. However, by using salt solutions at low concentrations in both the sink and the reservoir, we expect the change to be monotonic but small in our system.

To compare our experimental results quantitatively using the electrokinetic equations, Figure 1B, we modeled the transport of material in a dead-end pore and examined the tracer velocity (**u**) at any position (x) and any time (t).

$$\mathbf{u}(x, t) = \mathbf{v}(x, t) + \mathbf{U}_{dp}(x, t) \quad (2)$$

First we describe how we estimate the flow field (**v**) within the pore, and later we discuss the additional diffusiophoretic contribution ($\mathbf{U}_{dp}$) from the individual tracers. To evaluate **v** we model our system as a long, square capillary (Figure 1A) with a particular ζ_w and known D_+ and D_- of the ions. With the salt solution at the top (inner capillary) and DI water containing sPSL beads at the bottom (sink, outer capillary) (with no observed contribution to speeds from density gradients), we have temporal salt concentration gradients ($\partial n/\partial t \neq 0$) that are also spatially nonuniform ($\partial n/\partial x \neq 0$). We solve numerically for the concentration profile $n(x,t)$ in the system (see Supporting Information, Figure S3) using 1-dimensional, time-dependent Fick's law of diffusion[35] and thus estimating $\nabla n(x,t)$.

In the capillary, **v** is calculated using the concentration profile $n(x,t)$. First we evaluate $\mathbf{v}_{do}$ near the wall using eq 3 which is a combination of both the electroosmotic and the chemiosmotic flow. Both of these flow contributions are analogous to electrophoresis and chemiphoresis, respectively.[34]

$$\mathbf{v}_{do} = -\frac{\varepsilon}{\eta}\left\{\frac{kT}{Ze}\frac{D_+ - D_-}{D_+ + D_-}\zeta_w - \frac{2k^2T^2}{Z^2e^2}\ln\left[1 - \tanh^2\left(\frac{Ze\zeta_w}{4kT}\right)\right]\right\}\frac{\nabla n}{n} \quad (3)$$

Next, we calculated the complete diffusioosmotic flow profile, different from that of a plug flow in an open channel, which is evaluated using Bowen's[36] result. This result accounts for the fluid dynamics in a closed rectangular channel using the steady-state Stokes equation for the case when there is an electroosmotic slip velocity at the wall surfaces and the net flow across any cross-section of the channel is zero. The flow field has a parabolic shape[37] due to the back-pressure built in the dead-end section (Supporting Information, Figure S4). In most fluid mechanics problems, the wall resists flow due to the no-slip boundary condition. Here, the finite slip at the wall *drives* flow; that is, the wall is the "pump", and this sets up a flow field within the entire capillary.

The contribution from the independent rates of tracers ($\mathbf{U}_{dp}$) to eq 2 also needs to be assessed. We assumed sPSL beads which have a negative zeta potential (ζ_p), and therefore in a salt gradient, undergo diffusiophoresis[34,38] with the expression for $\mathbf{U}_{dp}$ being very similar to eq 3. ζ_w and ζ_p were measured independently. With all the parameters in the system being known, we substitute **v** and $\mathbf{U}_{dp}$ in eq 2 and are now able to compare our modeling results with experimental observed velocities, **u**, for different tracers (for details regarding modeling predictions and its subsequent validation with experiments, see Supporting Information). The data on electrokinetic transport of beads toward the high salt regime compare well with our TDOF model. As expected, the speeds of the beads decay both spatially and temporally (Figure 1B) with those near to the mouth of the pore (x = 250 μm) having speeds higher than those inside the pore (x = 400 μm). We also found that there is a negligible contribution to speeds coming from density differences, and hence, we reverted back to a simpler horizontal microscope setup for the rest of our experiments.

Particles or solutes with the same zeta potential can exist in various shapes and sizes. To investigate the contribution of changing sizes to transport in dead-end pores, we turned our attention toward the transport of hexadecane oil emulsions (diameters (ϕ) from 10 to 80 μm) out of dead-end-capillaries. For sPSL beads, since $|\zeta_p| > |\zeta_w|$, diffusiophoresis of the particle dominates the flow field in the capillary at all locations (Supporting Information, Figure S4). For oil emulsions, $|\zeta_e| < |\zeta_w|$, with $\zeta_e = -35$ mV the flow dominates over phoretic motion. The small emulsions, being entirely near the wall, are expected to move in the same direction as the diffusioosmotic flow at the wall ($\mathbf{v}_{do}$).

Large emulsions, which extend farther into the capillary, should move in the *opposite* direction. Thus, the direction of motion of oil emulsions is predicted to be a function of their diameter (Figures 2C and 3A).

The experimental observations bear out these predictions. Figure 2A is a schematic of the dead-end-capillary system with emulsions inside the pore and sPSL beads outside in the sink. We observed the transport of small oil emulsion droplets (roughly 20 μm diameter hexadecane emulsions stabilized with 2.0%$_{wt}$ Tween-20) out of the dead-end-capillary, *away* from the high salt concentrations; the sPSL beads and the larger emulsions (roughly 80 μm diameter) moved *toward* higher salt concentrations. In Figure 2B one sees that the fluid flow generates transport and exchange of sPSL beads and oil droplets in the system. The small emulsions that initially occupied the dead-end pore were transported toward the sink, whereas the beads moved in the opposite direction. This results in an exchange of material across the dead-end pore. These images were taken from the top surface of the capillary at all times with the gravity pointing into the figure and thus not playing a role in the horizontal motion of the emulsions. Figure 2C depicts the relative competition between emulsions of different sizes to move in or out of the dead-end pore. The isolated smaller emulsions can be seen to move toward the lower salt regime, whereas the bigger emulsions move and push the smaller emulsions in front of them toward the higher salt regime. Note that the electrolyte gradient and the resultant **E**-field point in different directions in Figure 2 panels B and C.

The size dependence of oil emulsions on their direction of motion underscores the effects of pore and particle sizes on the exchange process. While smaller emulsions can be easily extracted (since they move along the direction of the **E**-field), for efficient recovery the larger emulsions must be first reduced in size, perhaps through surfactant polymer flooding of oil wells.[39] As Figure 3 panels A and B illustrate, we show through both experiments and modeling that the movement of polydispersed oil emulsions depends on their placement inside the dead-end pore. To quantify the rates of oil extraction from our dead-end pores, we used the same electrokinetic model as we did for the tracer particles. Figure 3A shows the positioning of the polydispersed emulsions across the *xy* plane, and the circles in Figure 3B show their corresponding position along the *yz* plane. Smaller emulsions are closer to the top surface (the plane connecting {0,100} and {100,100}), whereas the larger emulsions are a little farther into the bulk. The parabolic nature of the fluid flow drives these emulsions along with it. The smaller emulsions ($\phi < 5\ \mu$m) are seen to move out with a speed of 1 μm/s (Figure 3B) (negative sign indicates motion toward the sink, while a positive sign shows movement in the opposite direction, toward the dead-end region). The relatively larger emulsions ($\phi > 40\ \mu$m) are seen to be stationary as predicted from our model. The really large

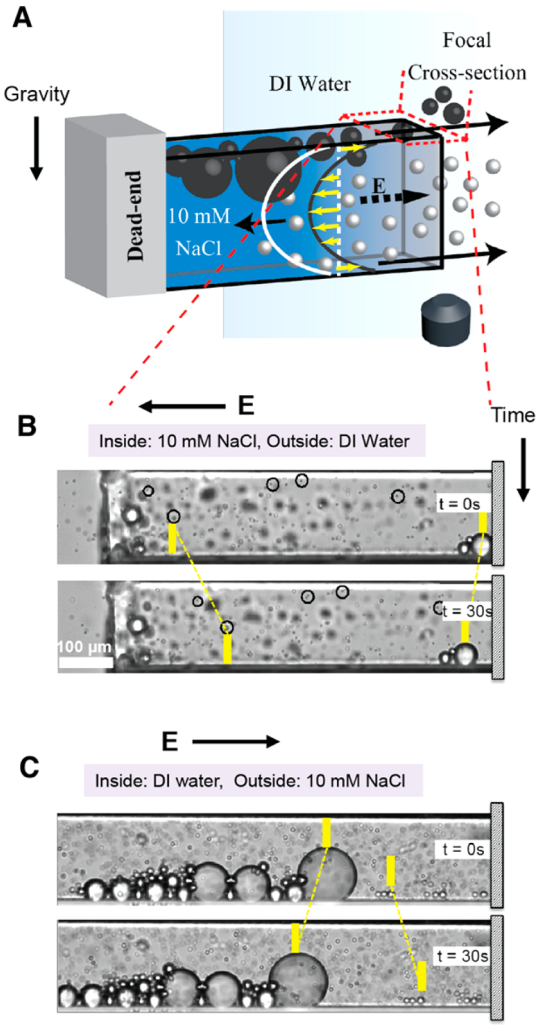

Figure 2. Polydispersity in oil emulsions resulting in transport into or out of dead-end pore. (A) Schematic of the experimental setup used to apply a salt gradient across a dead-end-capillary. The solid black arrows indicate the direction of fluid movement. We focus the inverted microscope to the top cross-section of the capillary in order to observe the motion of oil (gray spheres) and sPSL beads (white spheres). Gravity at all times is perpendicular to the direction of motion of oil emulsions. The smaller oil emulsions are found to move out of the capillary, whereas the larger oil emulsions and the sPSL beads are observed to move in. The yellow arrows show this motion of the oil emulsions along the parabolic flow profile (gray) while the white colored parabola indicates the path of sPSL beads. The black dashed lines give the E-field in the system. (B) Time-lapse images showing small emulsion droplets being driven away from the dead end, whereas the sPSL beads (small black circles) are diffusiophoretically transported toward the dead end. Both transport rates are predicted quantitatively by our model (Figure 3). Yellow bars indicate the position of these beads and emulsions before and after 30 s (Supporting Information, Video S5). The magnitud of the scale bar is 100 μm. (C) When the DI water is inside with salt outside, smaller emulsions ($\phi < 10\ \mu$m) move toward the dead end and larger emulsions ($\phi > 40\ \mu$m) move away from it (Video S6) demonstrating the reversible nature of transport.

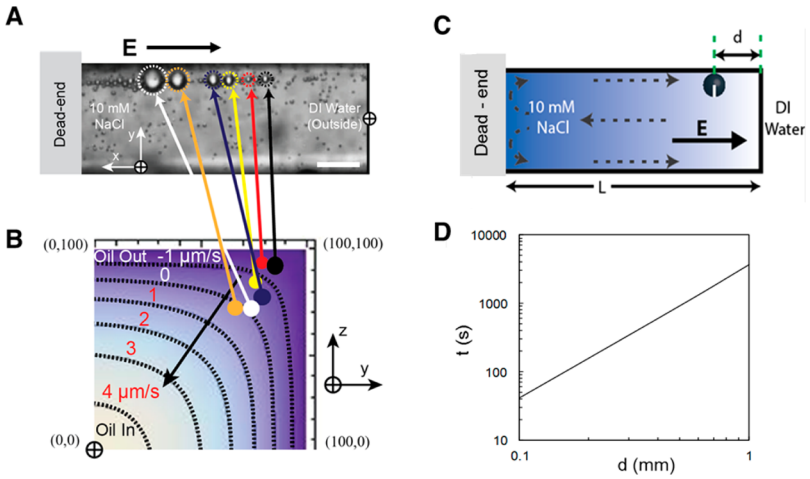

Figure 3. Transport rate for emulsions of various sizes and time scales out of a dead-end pore. (A,B) The speeds of emulsion droplets out of the dead-end pore were tracked and modeled at a distance of 200 μm away from the mouth of the pore. (scale bar = 100 μm). The smaller emulsions were seen to move toward the sink, both through experiments and modeling, at a speed of just over 1 μm/s, whereas the medium-sized emulsions were mostly stationary. Using the diffusiophoretic transport equations, the u for these emulsions was modeled (in B) with the color gradient signifying the direction of motion for these emulsions (negative sign indicates motion toward the sink, while the positive sign shows movement in the opposite direction, toward the dead-end region). In our calculations for B, $\zeta_e = -33$ mV, $\zeta_w = -65$ mV, $x = 200$ μm at $t = 300$ s. (C,D) The time taken for an emulsion of diameter = 20 μm to exit the dead-end pore as a function of its distance from the mouth of the pore (*d*, mm), as obtained from modeling. Times vary from a few seconds to hours depending on *d*. Large emulsions are predicted to be stuck in the dead-end pore which is indeed observed experimentally.

emulsions ($\phi \approx 80$ μm) (Figure 2C), which extend significantly into the bulk move toward the dead-end, a direction opposite to that observed for the small emulsions.

The time required for material exchange in these pores varies with distance from the mouth of the pore. Figure 3C shows the schematic of an oil emulsion located at a distance *d* away from the mouth of a dead-end pore of length *L*, which contains salt. Here, we modeled the time taken for this emulsion to come out of the pore if its diameter is 20 μm. As seen in Figure 3D, the time scales (calculated using eq 3 and Fickian diffusion) for extraction of this emulsion increases logarithmically with the log of the distance *d*, which indicates that this transport process is most effective if the emulsion is situated close to the mouth of the dead-end pore.

Most geologic systems contain complex mixtures of ions, including multivalent ions. We further extended our experiments to divalent ions, using saturated calcium carbonate (Supporting Information, Figure S5, Video S7) and carbonated water solutions (Figure S6). By using small emulsions with oleic acid as a steric stabilizer, we observed their motion in the water having a gradient of dissolved CO_2 (*i.e.*, bicarbonate ion, HCO_3^-). In such a setup, $\zeta_e = -60$ mV compared to $\zeta_w = -30$ mV (at pH ≈ 4). The emulsions are seen to behave like sPSL beads in NaCl gradient as they continue to move toward the higher HCO_3^- concentration regime. Similar behavior is observed for the gradient formed by calcium carbonate dissolution. Being able to control local solution conditions with dissolved CO_2

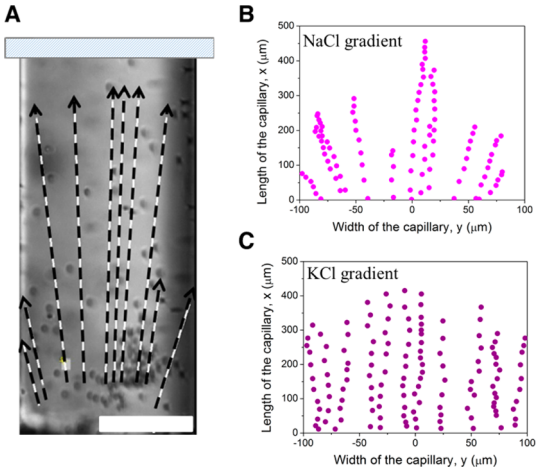

Figure 4. Transverse transport of beads inside dead-end pores. (A) Tracer particles tracked at $z = 0$ μm (center plane) entering the dead-end pore containing 10 mM NaCl solution from a DI water sink. (scale bar = 100 μm). The tracers are convected radially toward the walls and then slow down or accumulate along them. (B) The magenta colored dots follow the paths of individual beads entering the pore due to NaCl gradient from a DI water sink. The beads near to the walls of the dead-end pore are seen to execute a curved trajectory in comparison to the ones in the center. The slope of the trajectory increases (*i.e.*, the drift toward the wall increases) for the beads closest to the walls of the dead-end pore. The trajectories are symmetric about the central axis. (C) The purple colored dots track the route followed by individual beads entering the pore due to 10 mM KCl gradient from a DI water sink. The beads are observed to move in a predominantly linear path into the higher salt regime, except for the beads very close to the side walls of the dead-end pore. This observed phenomenon can be explained based the relative contributions of electrophoresis and chemiphoresis to the charged particle movement.

provides interesting opportunities, either for sequestration (*e.g.*, toxic or radioactive substances) or removal (*e.g.*, oil) of specific materials.

There is one more important aspect of TDOFs in our system: Convection dominates over diffusion for the beads, especially at distances less than 500 μm from the mouth of the capillary ($Pe_{beads} = Ua/D_{bead} \approx 1000$, where U refers to the velocity scale for the beads, a is the typical dimension of the bead, and D_{beads} is the diffusion coefficient for the beads in a dilute solution). In NaCl gradients, in addition to the axial motion of the sPSL beads discussed above, we also observe a transverse drift toward the side walls of the capillary in the dead-end pore setup (Figure 4A, Supporting Information, Video S8). The behavior has similarities to that presented in a recent modeling paper by Rubinstein and Zaltzman,[40] but in our case we have a spatially and temporally varying **E**-field in the system arising from the concentration gradients which drive transport. The trajectory of the sPSL beads tracked along the *yz*-plane (see Figure 4B) for the NaCl salt gradient (*e.g.*, 10 mM NaCl in the smaller capillary and 1 mM NaCl in the sink) is very different from that observed when KCl salt was used to create the same gradient (*i.e.*, 10 mM KCl in the smaller capillary and 1 mM KCl in sink) (Figure 4C). Beads in the KCl gradient undergo little lateral motion. Though the analysis needed to deconvolute the mechanism behind the radial drift from axial motion is beyond the scope of this article, we briefly discuss the physics behind such an observed phenomenon. Since the fluid flow profile is parabolic inside dead-end-capillaries, the concentration gradient can exist, mostly near the mouth of the pore, both along the *x*- and *y*-axis. This distribution of salt inside the pore generates an **E**-field also along the *y*-direction that can make the beads drift toward the side walls. The beads along the center line move straight due to the symmetry of the **E**-field. However, the observed lateral motion does not happen in the case of KCl gradients, where chemiphoresis and chemiosmosis are the only operating effects in the system, since K^+ and Cl^- have virtually identical diffusion coefficients and produce almost no **E** field.

CONCLUSION

We have shown that by employing locally available chemical energy—in the form of spatiotemporal ion gradients—transient diffusioosmotic flows (TDOFs) can be setup to perform mechanical work in hard-to-reach dead-end pores, resulting in exchange of materials across the pores. Our model accurately predicts our observations. Transient salt gradients are ubiquitous in biological and geological systems. Geological examples include flows originating in disturbed mineral formations[41] and geoengineering involving the creation of ion gradients for enhanced oil recovery.[42] In biology, TDOFs contribute to the movement of biomolecules to specific targets,[43] as well as other forms of intercellular transit.[44] In addition, TDOFs are also likely involved in patterns[45] formed from mineral precipitates. One interesting practical application is the design of a self-regulated drug delivery system where the release rate of the drug can be regulated as a function of the physiological change in salt concentration or pH.

MATERIALS AND METHODS

Materials. We prepared our salt solutions using the chemicals obtained from Sigma-Aldrich. Sodium chloride (NaCl) and potassium chloride (KCl) were dissolved in DI water (Millipore Corporation Milli-Q system, with a specific resistance of 1.8 MΩ-cm) to prepare various concentrations of stock solutions. Surfactant-free sulfate-functionalized polystyrene latex beads (sPSL, ϕ = 3.0 μm ± 2.1%; *w*/*v* = 8%) and surfactant-free amidine-functionalized polystyrene latex beads (aPSL, ϕ = 1.5 μm ± 2.4%; *w*/*v* = 4%) were purchased from Interfacial Dynamics Corporation (Portland, OR). Fluorescent sPSL beads (ϕ = 4 μm; excitation/emission, 580 nm/605 nm) and fluorescent amine-functionalized beads (ϕ = 2 μm; excitation/emission, 505 nm/515 nm) were used to trace the flow profile under a confocal microscope. Emulsions were prepared by an oil-in-water emulsion process using hexadecane (Sigma-Aldrich) with 2% Tween-20 (Sigma-Aldrich) acting as a stabilizer. The polydispersity in the emulsions was varied by changing mixing times and rates of mixing.

Design of Dead-End Capillaries and Their Operation. Our dead-end pore systems were composed of two capillaries, with a smaller one placed inside the larger. Borosilicate square glass capillaries (part no. 8320-050 and 8290-050) used in our experiments were purchased from Vitrocom (Mountain Lakes, NJ) with the larger capillary (height, h = 0.9 mm) forming the sink and the smaller capillary (h = 0.2 mm) making up the dead-end reservoir in our system. The reservoir mostly contained the salt (sometimes with emulsions), whereas the sink contained DI water with sPSL beads. To create the dead-end setup, the sink was first filled with DI water solution, sealed at one end with paraffin wax and placed on a clear glass slide. The smaller capillary, with the salt solution in it, was then inserted inside the larger closed capillary (Supporting Information, Figure S1) and waxed across the open ends. The motion of beads and emulsions were observed across the open-end of the smaller capillary under an optical transmission microscope with different magnifications.

Characterization Techniques. We used both an inverted light microscope and a confocal microscope to image our systems. Brightfield observation of particle motion was made on a Nikon inverted microscope (Eclipse TE2000-U) fitted with an optical light source and CCD camera (Q-Imaging). Nikon NIS Elements Imaging Software (V. 4) was used for both particle and emulsion velocity measurements and tracking. A Leica TCS SP5 laser scanning confocal microscope (LSCM, Leica Microsystems) was used for imaging and recording the motion of fluorescent particles. Observations were made at 10× magnification for most cases. Image intensity profiles were analyzed using ImageJ software (National Institutes of Health).

Zeta Potential Measurements of Latex Particles. For zeta potential (ζ) measurements of sPSL tracers (both fluorescent and non-fluorescent), amidine-functionalized PSL tracers and amine-functionalized PSL fluorescent tracers, we used a Zetasizer Nano ZS90 (Malvern, MA, model ZEN3690) equipment. The ζ-potential of the particles were measured at 298 K using disposable cuvettes (DTS1061) at ionic strengths of 0.1–100 mM salt concentration and pH of 5.8. Zeta potential of

the borosilicate capillary, at different ion concentrations, was obtained from the literature.[46]

Modeling. To model diffusiophoresis and diffusioosmosis, we used the electrokinetic equations, which consist of the Stokes equations, ion migration equations, continuity equations, and Poisson equation of electrostatics. The concentration gradient (∇n) was solved using Fick's second law of diffusion, and it gives rise to an **E**-field mentioned earlier, due to a difference in diffusion coefficients (D_i).

Conflict of Interest: The authors declare no competing financial interest.

Acknowledgment. We thank Dr. K. Bishop for his insightful suggestions. This work was funded by the Advanced Energy Consortium and, in part, by the Air Force Office of Scientific Research (FA9550-10-1-0509).

Supporting Information Available: Supplementary methods, theory, modeling, and supporting videos. This material is available free of charge *via* the Internet at http://pubs.acs.org.

REFERENCES AND NOTES

1. Lake, L. W. *Enhanced Oil Recovery*; Prentice Hall, 1989.
2. RezaeiDoust, A.; Puntervold, T.; Strand, S.; Austad, T. Smart Water as Wettability Modifier in Carbonate and Sandstone: A Discussion of Similarities/Differences in the Chemical Mechanisms. *Energy Fuels* **2009**, *23*, 4479–4485.
3. Jerauld, G. R.; Brodie, J. A. Impact of Salt Diffusion on Low-Salinity Enhanced Oil Recovery. In *SPE Improved Oil Recovery Symposium*; Society of Petroleum Engineers: Richardson, TX, 2014.
4. Suski, B.; Revil, A.; Titov, K.; Konosavsky, P.; Voltz, M.; Dagès, C.; Huttel, O. Monitoring of an Infiltration Experiment Using the Self-Potential Method. *Water Resour. Res.* **2006**, *42*, W08418.
5. Yoshida, S. Convection Current Generated Prior to Rupture in Saturated Rocks. *J. Geophys. Res.: Solid Earth* **2001**, *106*, 2103–2120.
6. Pride, S. R.; Morgan, F. D. Electrokinetic Dissipation Induced by Seismic Waves. *Geophysics* **1991**, *56*, 914–925.
7. Jouniaux, L.; Ishido, T. Electrokinetics in Earth Sciences: A Tutorial. *Int. J. Geophys.* **2012**.
8. Syková, E.; Nicholson, C. Diffusion in Brain Extracellular Space. *Physiol. Rev.* **2008**, *88*, 1277–1340.
9. Safford, R. E.; Bassingthwaighte, E. A.; Bassingthwaighte, J. B. Diffusion of Water in CAT Ventricular Myocardium. *J. Gen. Physiol.* **1978**, *72*, 513–538.
10. Bear, J. *Dynamics of Fluids in Porous Media*; American Elsevier Publishing Company: New York, 1972; pp 44−45.
11. Fuerstman, M. J.; Deschatelets, P.; Kane, R.; Schwartz, A.; Kenesis, P. J. A.; Deutch, J. M.; Whitesides, G. M. Solving Mazes Using Microfluidic Networks. *Langmuir* **2003**, *19*, 4714–4722.
12. Goodknight, R. C.; Klikoff, W. A.; Fatt, I. Non-steady-state Fluid Flow and Diffusion in Porous Media Containing Dead-End Pore Volume 1. *J. Phys. Chem.* **1960**, *64*, 1162–1168.
13. Dagdug, L.; Berezhkovskii, A. M.; Makhnovskii, Y. A.; Zitserman, V. Y. Transient Diffusion in a Tube with Dead Ends. *J. Chem. Phys. Phys.* **2007**, *127*, 224712.
14. Stone, H. A.; Stroock, A. D.; Ajdari, A. Engineering Flows in Small Devices: Microfluidics toward a Lab-on-Chip. *Annu. Rev. Fluid Mech.* **2004**, *36*, 381–411.
15. Squires, T. M.; Quake, S. R. Microfluidics: Fluid Physics at the Nanoliter Scale. *Rev. Mod. Phys.* **2005**, *77*, 977–1026.
16. Whitesides, G. M. The Origins and the Future of Microfluidics. *Nature* **2006**, *442*, 368–373.
17. Hunter, R. J. *Zeta Potential in Colloid Science*; Academic: New York, 1981; pp 386.
18. McDermott, J. J.; Kar, A.; Daher, M.; Klara, S.; Wang, G.; Sen, A.; Velegol, D. Self-Generated Diffusioosmotic Flows from Calcium Carbonate Micropumps. *Langmuir* **2012**, *28*, 15491–15497.
19. Laser, D. J.; Santiago, J. G. A Review of Micropumps. *J. Micromech. Microeng.* **2004**, *14*, R35–R64.
20. Baaske, P.; Weinert, F. M.; Duhr, S.; Lemke, K. H.; Russell, M. J.; Braun, D. Extreme Accumulation of Nucleotides in Simulated Hydrothermal Pore Systems. *Proc. Nat. Acad. Sc. U.S.A.* **2007**, *104*, 9346–9351.
21. Derjaguin, B. V.; Sidorenko, G. P.; Zubashenko, E. A.; Kiseleva, E. V. Kinetic Phenomena in Boundary Films of Liquids. *Kolloidn Zh.* **1947**, *9*, 335–348.
22. Dukhin, S. S.; Derjaguin, B. V.; Matievich, E. *Electrokinetic Phenomena. Surface and Colloid Science*; John Willey and Sons: New York, Toronto 1974; Vol. 7.
23. Prieve, D. C.; Anderson, J. L.; Ebel, J. P.; Lowell, M. E. Motion of a Particle Generated by Chemical Gradients. Part 2. Electrolytes. *J. Fluid Mech.* **1984**, *148*, 247–269.
24. Anderson, J. L.; Malone, D. M. Mechanism of Osmotic Flow in Porous Membranes. *Biophys. J.* **1974**, *14*, 957–982.
25. Chiang, T. Y.; Velegol, D. Multi-ion Diffusiophoresis. *J. Colloid. Interface Sci.* **2014**, *424*, 120–123.
26. Ebel, J. P.; Anderson, J. L.; Prieve, D. C. Diffusiophoresis of Latex Particles in Electrolyte Gradients. *Langmuir* **1988**, *4*, 396–406.
27. Abecassis, B.; Cottin-Bizonne, C.; Ybert, C.; Ajdari, A.; Bocquet, L. Boosting Migration of Large Particles by Solute Contrasts. *Nat. Mater.* **2008**, *7*, 785–789.
28. Siria, A.; Poncharal, P.; Biance, A. L.; Fulcrand, R.; Blasé, X.; Purcell, S. T.; Bocquet, L. Giant Osmotic Energy Conversion Measured in a Single Transmembrane Boron Nitride Nanotube. *Nature* **2013**, *494*, 455–458.
29. Lee, C.; Cottin-Bizonne, C.; Biance, A. L.; Joseph, P.; Bocquet, L.; Ybert, C. Osmotic Flow through Fully Permeable Nanochannels. *Phys. Rev. Lett.* **2014**, *112*, 244501.
30. Khair, A. S.; Squires, T. M. The Influence of Hydrodynamic Slip on the Electrophoretic Mobility of a Spherical Colloidal Particle. *Phys. Fluids* **2009**, *21*, 042001.
31. Prieve, D. C.; Gerhart, H. L.; Smith, R. E. Chemiphoresis—A Method for Deposition of Polymer Coatings without Applied Electric Current. *Ind. Eng. Chem. Prod. Res. Dev.* **1978**, *17*, 32–36.
32. Anderson, J. L. Colloid Transport by Interfacial Forces. *Annu. Rev. Fluid Mech.* **1989**, *21*, 61–99.
33. Florea, D.; Musa, S.; Huyghe, J. M. R.; Wyss, H. M. Long-Range Repulsion of Colloids Driven by Ion Exchange and Diffusiophoresis. *Proc. Natl. Acad. Sci. U.S.A.* **2014**, *111*, 6554–6565.
34. Kim, Y.; Shah, A. A.; Solomon, M. J. Spatially and Temporally Reconfigurable Assembly of Colloidal Crystals. *Nat. Commun.* **2014**, *5*.
35. Bird, R. B.; Stewart, W. E.; Lightfoot, E. N. *Transport Phenomena*; John Wiley & Sons; New York, 2001.
36. Bowen, B. D. Effect of a Finite Half-width on Combined Electroosmosis-Electrophoresis Measurements in a Rectangular Cell. *J. Coll. Int. Sc.* **1981**, *82*, 574–576.
37. Hunter, R. J. Measurement of Electrokinetic Parameters. In *Zeta Potential in Colloid Science*; Academic Press, Inc.: London and New York, 1981.
38. Kar, A.; Guha, R.; Dani, N. S.; Velegol, D.; Kumar, M. Particle Deposition on Microporous Membranes Can Be Enhanced or Reduced by Salt Gradients. *Langmuir* **2014**, *30*, 793–799.
39. Seethepalli, A.; Adibhatia, B.; Mohanty, K. K. Physicochemical Interaction during Surfactant Flooding of Fractured Carbonate Reservoirs. *SPE J.* **2004**, *9*, 411–418.
40. Rubinstein, I.; Zaltzman, B. Convective Diffusive Mixing in Concentration Polarization: From Taylor Dispersion to Surface Convection. *J. Fluid Mech.* **2013**, *728*, 239–278.
41. Putnis, A. Replacement Process. *Geochem. Persp.* **2012**, *1*, 388–402.
42. Lager, A.; Webb, K. J.; Collins, I. R.; Richmond, D. M. LoSal Enhanced Oil Recovery: Evidence of Enhanced Oil Recovery at the Reservoir Scale. In *SPE Symposium on Improved Oil Recovery*; Society of Petroleum Engineers: Richardson, TX, 2008.
43. Yadav, V.; Freedman, J. D.; Grinstaff, M.; Sen, A. Bone-Crack Detection, Targeting, and Repair Using Ion Gradients. *Angew. Chem., Int. Ed.* **2013**, *125*, 1–6.
44. Sui, H.; Han, B. G.; Lee, J. K.; Walian, P.; Jap, B. K. Structural Basis of Water-Specific Transport through the AQP1 Water Channel. *Nature* **2001**, *414*, 872–878.

45. Noorduin, W. L.; Grinthal, A.; Mahadevan, L.; Aizenberg, J. Rationally Designed Complex, Hierarchical Microarchitectures. *Science* **2013**, *340*, 832–837.
46. Barz, D. P. J.; Vogel, M. J.; Sheen, P. H. Determination of the Zeta Potential of Porous Substrates by Droplet Deflection. I. The Influence of Ionic Strength and pH Value of an Aqueous Electrolyte in Contact with a Borosilicate Surface. *Langmuir* **2009**, *25*, 1842–1850.